An experimental investigation on dynamics of turbulent non-premixed swirling oxygen-enriched flames

N. Merlo[1], T. Boushaki[*,1,2], C. Chauveau[1], I. Gökalp[1]

[1] ICARE CNRS, 1C, Avenue de la Recherche Scientifique, 45071 Orléans Cedex 2, France
[2] Université d'Orléans, IUT, GTE – 45067 Orléans cedex 2, France

Abstract

The current paper describes the dynamics of flow and turbulent non-premixed swirling oxygen-enriched flames. The experiments are conducted with a 25 kW combustion chamber. The burner configuration explored in this work is a co-axial swirl stabilized burner used in the turbulent regime. Multiple stereo-PIV planes (longitudinal and transverse planes) are extensively used to characterize the flow field in non-reacting and reacting conditions. Results show that combustion noticeably affects the swirling motion and increase the backflow rate in the recirculation zone. The entrainment rate measurements explain one possible mechanism for the decrease of the NO_x emissions when the global equivalence ratio increases via an increase of the entrainment rate at the base of the flame.

Introduction

Swirl flows are extensively used to enhance mixing and improve flame stabilization in a variety of practical situations involving low calorific fuel, fuel spray, coal and biomass [1]. Strongly swirling reacting flow benefits are now well-known: flame stabilization enhancement due to the vortex breakdown phenomenon, responsible for the central recirculation zone (CRZ) occurrence [2-5], turbulent mixing improvements due to the Precessing Vortex Core (PVC) [6, 7].

Besides, fuel injection geometry plays a major role in flame stabilization as studied by many authors [8, 9]. Considering swirling annular jets and non-premixed flames, fuel radial injection allows a better mixing than axial injection [10, 11] at the close vicinity of the burner exit. Nevertheless, such turbulent swirling lean flames exhibit high sensitivity to combustion instabilities [12-14]. Oxygen enrichment of the oxidizer appears as an effective way to reduce flame instabilities combining a more efficient combustion with an extension of flame stability limits [15, 16]. Combining effects of fuel radial injection, swirling motion and oxygen enrichment are not well understood. Previous experimental studies of these types of turbulent swirling flames were limited to pollutant emissions, flame temperatures, and heat transfer characteristics [17, 18].

In the present paper, an experimental study of a 20 kW burner is proposed focusing on its dynamic features in isothermal and reacting conditions. A previous work [16] described an experimental study carried out on the same burner to assess the oxygen enrichment effects on flame stability and pollutant formation. Flame stabilization regimes were first identified for axial and swirling jets with and without oxygen enrichment. Flame lift-off heights were also quantified varying the swirl intensity, the oxygen enrichment rate and the global equivalence ratio.

In particular, the NO_x emissions were shown to decrease with increasing the global equivalence ratio.

The flame dynamics is now investigated with stereo-PIV diagnostic, which is relevant for strongly three-dimensional flows. Topology of the instantaneous and mean flow is investigated in non-reacting and reacting conditions in order to identify the main regions of the swirling jet. Turbulent fluctuations are also exhibited in the two cases. The coupling between the entrainment rate of the surroundings and the flame lift-off height is presented as a scenario to explain the decrease of the NO_x emissions when the global equivalence ratio increases, based on the available literature and the results presented here.

Experimental facility and techniques

Burner and swirler

The burner used in this study consists of two concentric tubes with a swirler placed in an annular arrangement, which supplied the oxidant flow (air or oxygen-enriched air) as shown in Fig. 1 (a) and (b). Eight guide vanes were designed with various vane angles in order to[16] induce swirl with varying levels of intensity. The central pipe delivers fuel (methane) radially through eight holes symmetrically distributed along the periphery of the tube, just below the burner exit plane.

The degree of swirl for rotating flows is usually characterized by the non-dimensional swirl number S_n, which represents the ratio of the angular momentum flux G_θ, and the axial momentum flux G_z. times a characteristic distance of the radial dimension R (for example the outlet radius R_b)

* Corresponding author: toufik.boushaki@cnrs-orleans.fr

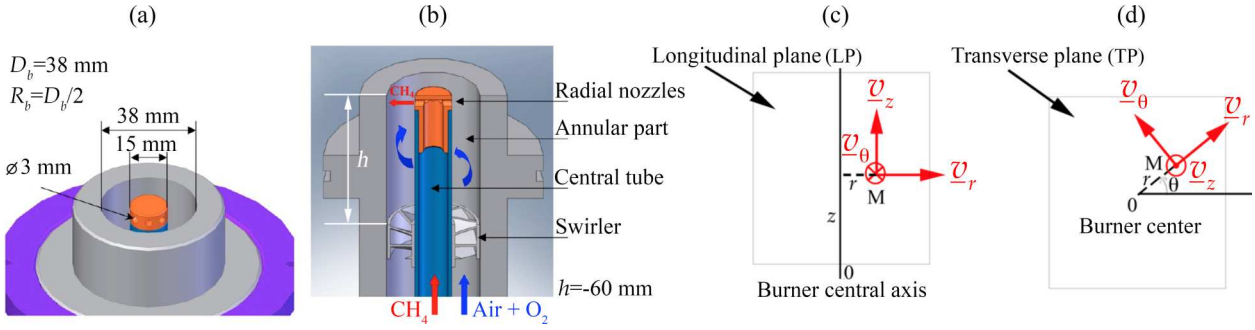

Fig. 1 Burner configuration: (a) 3D view of the top of the co-axial swirl burner; (b) Longitudinal section of the burner; (c) Velocity components in a longitudinal plane (LP); (d) Velocity components in a transverse plane (TP).

In the present work, it is defined as follows:

$$S_n = \frac{G_\theta}{RG_z} \quad (1)$$

The geometrical swirl number S_{ng} related to this configuration is defined as [19]:

$$S_{ng} = \frac{1}{1-\Psi}\left(\frac{1}{2}\right)\frac{1-\left(\frac{R_h}{R}\right)^1}{1-\left(\frac{R_h}{R}\right)^2}\tan(\alpha_0) \quad (2)$$

where Ψ is the blockage factor and α_0 is the vane angle. R and R_h are nozzle and vane pack hub radii respectively. A global equivalence ratio, Φ, can be defined as the molar ratio of methane and oxidant flows at injection to the molar ratio of methane and oxidant at stoichiometric conditions. An oxygen-air mixture is employed as the oxygen-enriched oxidizer flow. Mass flow rates of air, oxygen and fuel are regulated by thermal mass flow controllers. The measurements are performed for oxygen concentrations ranging from 21 to 30 % in volume, with geometrical swirl numbers of 0.8 and 1.4, and for global equivalence ratios of 0.8, 0.9 and 1. Table 1 summarizes the mass flow rates of the reactants as a function of the oxygen enrichment. The Reynolds number in the annular part, based on D_b and the bulk velocity, varies from 7,700 up to 8,300. The input power, on a Lower Heating Value (LHV) basis, varies from 12 up to 22 kW.

Table 1
Operating conditions

% O_2 (vol.)	Φ (-)	CH_4 mass flow rate (g/s)	O_2 mass flow rate (g/s)	Air mass flow rate (g/s)
21	0.80	0.24	0	5.2
25	0.80	0.29	0.30	5.0
30	0.80	0.35	0.70	4.6
21	0.90	0.27	0	5.2
25	0.90	0.33	0.30	5.0
30	0.90	0.39	0.70	4.6
21	1.0	0.31	0	5.2
25	1.0	0.36	0.30	5.0
30	1.0	0.44	0.70	4.6

The swirling flame takes place inside a combustion chamber with a square cross-section of 48 x 48 cm^2 and a height of 1 m that operated at atmospheric pressure. The walls of the combustion chamber were water cooled on the outside and refractory-lined inside. Six quartz windows were configured on each face of the chamber allowing optical access to all the potential flame zones.

Measurement techniques

Because of the strongly three-dimensional characteristics of the flow field structures, Stereo Particle Image Velocimetry (S-PIV) is used to gain insight into the flow field under non-reacting and reacting conditions. Four measurement planes were investigated at the burner exit: a longitudinal plane (LP) and three transverse planes (TP) at z/D_b=0.3, z/D_b=0.8, and z/D_b=1.3. The radial, azimuthal and axial velocity components, respectively noted (v_r, v_θ, v_z), are illustrated in Fig.1 (c) and (d) for each plane above mentioned in cylindrical coordinates. Fig. 2 shows the measurement plane arrangements.

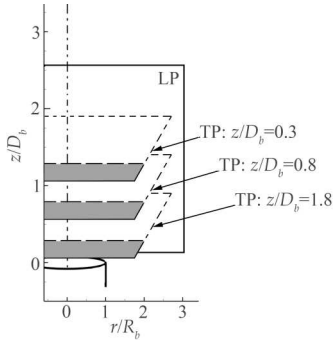

Fig. 2 S-PIV measurement plane locations in non-reacting and reacting conditions.

A double-pulsed Nd:YAG laser (Minilite 25 mJ/pulse) with a wavelength of 532 nm operating at 10 Hz is used as the light source. An optical system with a plano-convex cylindrical lens (focal length of 12.7 mm) and a spherical lens (focal length of 592 mm) transforms the laser beam into a laser sheet of about 500 µm thickness and about 100 mm height at the centre of the measurement window. The laser and the optical system are arranged along a transverse system axis to

perform different transverse planes. Synchronisation between the cameras and the laser is achieved by means of a TSI synchroniser Laser Pulse 610035. The mean time between two successive frames varies from 20 to 30 µs depending on operating conditions. The two cameras mounted on Scheimpflug adapters (TSI Powerview Plus 4MP, 12-bit output and 2048 x 2048 pixels^2) are oriented on the same side of the laser sheet. The angle between the two cameras is limited to 30° because of optical access limitations for measurements in the longitudinal measurement plane whereas for the transverse configuration, the angle is up to 60°. Nikon AF Micro-Nikkor 105 mm F/2.8 lenses and band-pass filters centered at 532 nm with a 10 nm bandwidth (50 %) are used to collect Mie particle scattering. A precision-machined twin level calibration target with dot pattern, perfectly centred over the burner inner diameter, is used for calibration. A host computer captures up to 1000 pairs of image frames for each camera continuously. Each frame covers a flow area of about 115 mm (width) x 95 mm (height) for the longitudinal configuration and about 90 mm x 90 mm for the transverse arrangement. TSI Insight 3G software is used to analyse S-PIV images and a background extraction scheme is applied to reacting case images as pre-processing step. The Al_2O_3 particles used for seeding the flow are 0.75 µm in diameter. Considering 32×32 pixels interrogation cells, a magnification ratio of 0.11 and 50 % overlap grid spacing, a typical spatial resolution achieved for the velocity vector grid is 1.1 mm in both directions.

Average characteristics of the flame

Velocity field topology

The first phase of the experimental work was to perform stereo-PIV measurements in non-reacting and reacting cases to better characterize the flow topology, observed in different planes as shown in Fig. 2. The operational conditions are those indicated in Table 1. In non-reacting conditions, N_2 is used instead of CH_4 but the N_2 flow rate is adjusted to keep an equivalent momentum at the exit of the fuel injection holes. Fig. 3 shows instantaneous velocity fields for non-reacting (NREAC) and reacting (REAC) conditions (air combustion) in longitudinal (LP) and transverse (TP) planes for Φ=0.8 and S_{ng}=1.4. The characteristic radius of the round swirling jet, defined as the distance between the jet center and the external jet position where the axial velocity v_z is equal to 0 ± 0.05 m/s, is increased by roughly 30 % because of the thermal volume expansion induced by combustion at all z/D_b positions. Besides, the axial velocity is locally higher in the reacting case (up to 13 m/s), which leads to higher axial velocity gradients along the radial axis in the reacting case. The CRZ region is clearly broadened in the radial direction and is intensified with the flame. One can notice a slight shift of the jet rotation center from the geometric center only in Fig. 3b, which could be the trace of the PVC on the instantaneous jet. This unsteady structure seems to be damped in reacting conditions as shown by other authors [1, 20]. The mean flow topology is described in Fig 4 by combining the different measurement planes. In reacting conditions, the azimuthal velocity is shifted toward the jet central axis. This shift occurs when z/D_b equal to or greater than 0.9 which corresponds to the flame lift-off height determined by OH^* chemiluminescence as reported in [16].

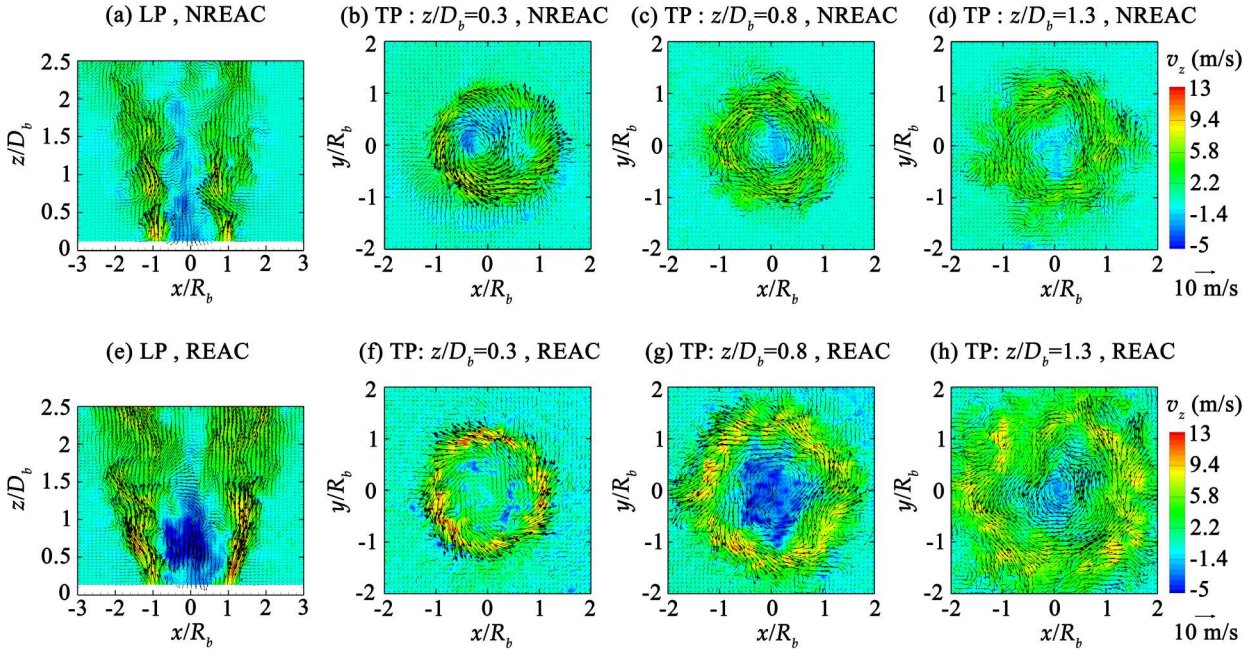

Fig. 3 Contours of instantaneous axial velocity v_z: in a longitudinal plane (LP) (a) in non-reacting (NREAC) and (e) in reacting conditions (REAC); in three different transverse planes (TP) for z/D_b=0.3 ((b) in NREAC and (f) in REAC), for z/D_b=0.8 ((c) in NREAC and (g) in REAC), for z/D_b=1.3 ((d) in NREAC and (h) in REAC). Air combustion case, Φ=0.8; S_{ng}=1.4.

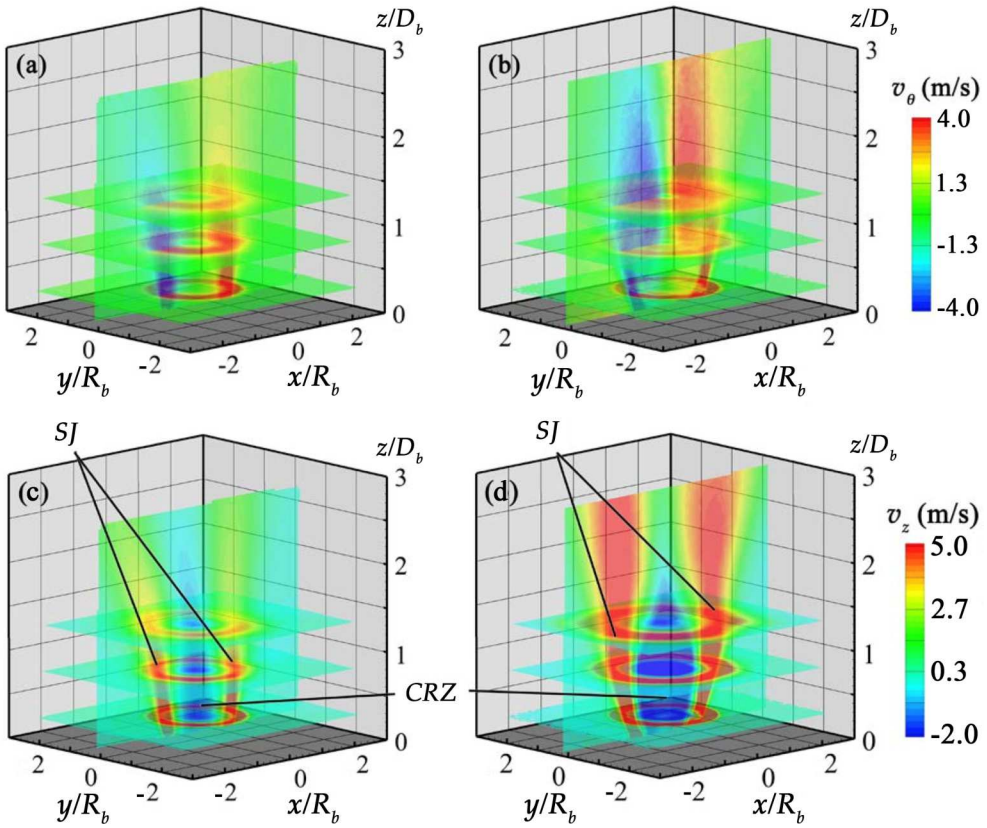

Fig. 4 Contours of mean velocity as a function of r/R_b and z/D_b: mean azimuthal velocity v_θ (a) NREAC, (b) REAC; mean axial velocity v_z (c) NREAC, (d) REAC. Air combustion case, Φ=0.8; S_{ng}=1.4. The velocity ranges are chosen to highlight the Swirling Jet (SJ) and the Central Recirculation Zone (CRZ) in the flow.

Figures 4 (c) and (d) illustrate the shape of the flow in both cases. The swirling jet (SJ) and the CRZ are clearly identified. The latter shows a recirculation bubble shape in the reacting case surrounded by a swirling jet accelerated by the flame via the increase of the axial velocity.

In reacting conditions, turbulence intensity, estimated via the normalized turbulence intensity, reaches higher levels at the jet central axis, than in the isothermal jet case as shown in Fig. 5. The high turbulence intensity region begins from the top of the CRZ and it expands further downstream.

Turbulent kinetic energy

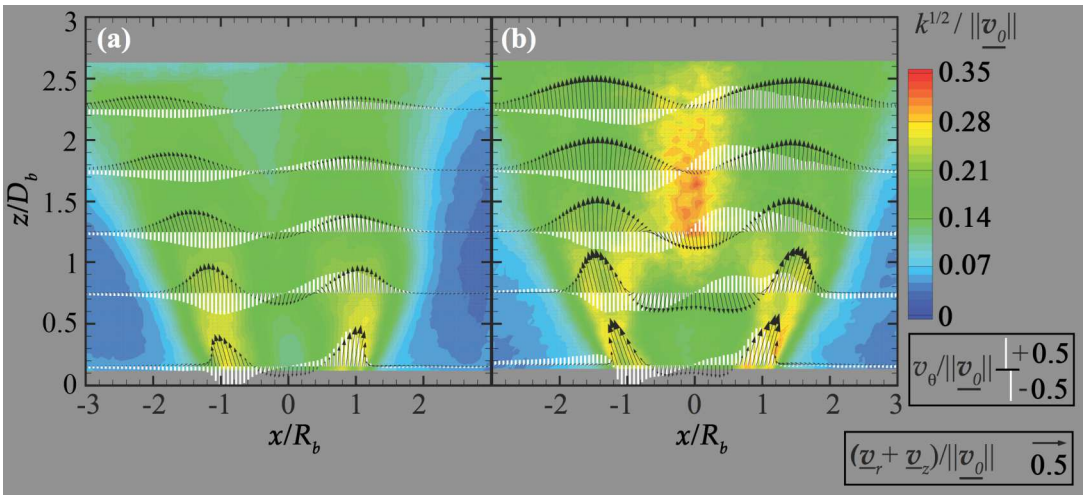

Fig. 5 Contours of normalized turbulent kinetic energy: (a) NREAC; (b) REAC. Vectors are underlined. v_0 is the maximum measured velocity at the vicinity of the burner exit. White bars at different z/D_b positions represent normalized azimuthal velocities. Black arrows represent the composition of the normalized radial and axial vectors. Air combustion case, Φ=0.8; S_{ng}=1.4.

It is found that the azimuthal turbulence rate, q_θ, defined as the ratio between the azimuthal velocity RMS fluctuations and the mean axial velocity, is mainly responsible for the higher turbulence levels in the central region of the swirling jet. Fig. 6 shows the radial profiles of q_θ at different z/D_b positions for both cases.

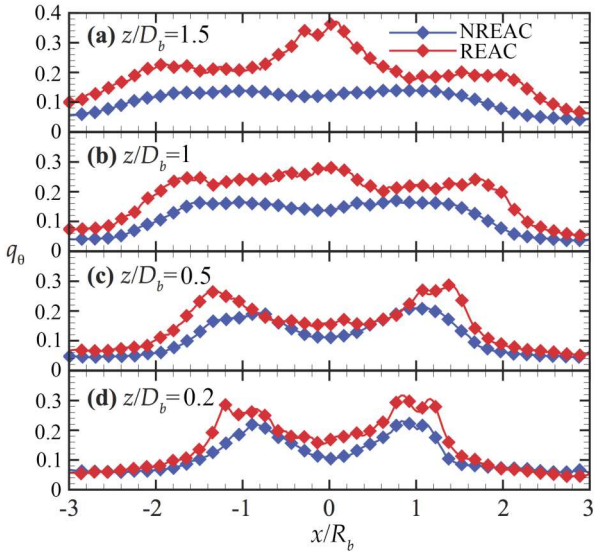

Fig. 6 Radial profiles of the azimuthal turbulence rate q_θ for NREAC (blue lines and diamonds) and REAC (red lines and diamonds) conditions at different z/Db positions: (a) z/D_b=1.5; (b) z/D_b=1; (c) z/D_b=0.5; (d) z/D_b=0.2.

Figure 6 shows that, in non-reacting conditions, the q_θ radial distribution reveals a bimodal distribution, which is specific to the burner exit geometry with a central bluff-body and an annular swirled flow. Downstream, q_θ tends to be constant along the radial axis in the swirling jet. In reacting conditions, the q_θ radial distribution follows the same distribution with higher intensities before the flame front namely for z/D_b equal to or smaller than 0.9. Figure 6 (a) and (b) show that, after the flame front, q_θ strongly increases close the jet central axis. This trend may be related to the flame-induced turbulence but also to the azimuthal velocity fluctuations via intermittency.

Entrainment rate

Methodology

Considering an axisymmetric jet flow, the jet entrainment rate per mass unit τ_e is defined as [21]:

$$\tau_e = \lim_{r\to\infty} \int_0^{2\pi} v_r r \,\mathrm{d}\theta = 2\pi \lim_{r\to\infty} r v_r \qquad (1)$$

In practice, we can pick a control surface, which contains the whole jet flow [22]. In this study, considering the specific flow structure, the relevant control surface is localized at the external jet where the axial velocity v_z is equal to 0 ± 0.05 m/s as illustrated in Fig. 7:

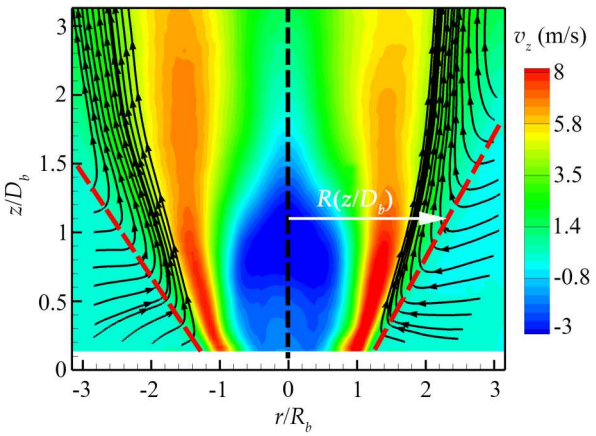

Fig. 7 Contours of axial velocity v_z in a longitudinal plane. Some streamlines are represented in black lines and arrows to emphasize the entrainment process from the surroundings to the jet. The red dotted lines correspond to the frontier of the control surface in the cutting plane. The central axe of the jet is in black dotted line. Oxygen content in the oxidizer: 25 % O_2, Φ=0.8; S_{ng}=1.4.

Therefore, the jet entrainment rate per mass unit τ_e can be rewritten as:

$$\tau_e(R(z)) = \lim_{r\to R(z)} \int_0^{2\pi} r v_r \,\mathrm{d}\theta \qquad (2)$$

$$= 2\pi R(z) v_r(R(z), z) \qquad (3)$$

Then it is convenient to define the non-dimensional entrainment rate Ψ as:

$$\Psi = \frac{M_e(z)}{M_0} = \frac{\int_{z_{min}}^{z} \rho\, \tau_e(R(z))\,\mathrm{d}z}{M_0} \qquad (4)$$

where M_0 and $M_e(z)$ correspond respectively to the initial (z=0) and the entrained mass flow rates from z_{min} to z. Stereo-PIV measurements at the very close vicinity of the burner exit plane were quite delicate mainly because of the potential laser light reflections on the burner exit throat surface. Consequently, stereo-PIV measurement fields start from z/D_b=0.12. The entrained surroundings are thus neglected for z/D_b ranges from 0 to 0.12. The axisymmetric assumption is verified using the transverse planes and the variability of the entrainment rate is assessed for different angular position.

Mixing dilution before the flame front

This section aims to assess the entrainment rate of the surroundings by the swirling jet. This may give more insight in the pollutant formation for non-premixed lifted flames. This section focuses on the NO_x

evolution with global equivalence ratio, by taking into account the mixture dilution before the flame front.

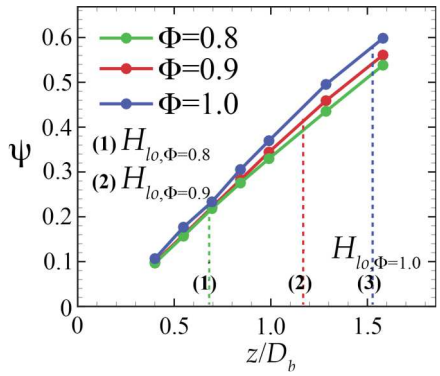

Fig. 8 Entrainment rate Ψ along the z/D_b axis for three equivalence ratios 0.8, 0.9 and 1. The lift-off heights are also reported in this figure [16].

Figure 8 shows that the normalized lift-off height H_{lo} increases from 0.7 to 1.5 with increasing the global equivalence ratio from 0.8 to 1. Figure 8 shows also that the entrainment rate linearly increases when z/D_b increases with a slight dependence to the global equivalence ratio. In particular, the entrainment rate slightly increases with increasing the global equivalence ratio at a given z/D_b position. These trends show that when the flame is anchored more downstream, the mixture brought to the flame base is more diluted by the surroundings, which are mainly composed with CO_2 and H_2O in a confined environment. This mechanism could lead to a decrease of flame temperature. A previous study [16] showed that the NO_x emissions, via the thermal pathway, decrease with increasing the global equivalence ratio from 0.8 to 1. Therefore, the increase of entrained surroundings to the base of the flame when the global equivalence ratio increases could explain the NO_x emission trend.

Conclusions

A laboratory-scale co-axial swirling burner, with methane radial injection, has been studied experimentally using stereo-PIV (SPIV) to characterize the flow topology in non-reacting and reacting cases. First, in reacting conditions, the central recirculation zone (CRZ) is intensified and shows a bubble shape compared to the isothermal case. Azimuthal mean velocity reveals a bifurcation of the maxima towards the jet central axis crossing the flame front. Moreover, the turbulence intensity levels are higher at the top of the CRZ and at the vicinity of the jet central axis. The entrainment rate is also estimated for three global equivalence ratios in order to explain the decrease of NO_x emissions with increasing the global equivalence ratio.

Acknowledgements

This work has been supported by the ANR (Agence National de la Recherche), project CO_2 Energicapt (ANR-10-EESI-0003).

References

[1] A. K. Gupta; D. G. Lilley; N. Syred, Swirl flows, Abacus Press, 1984.
[2] D. Feikema; R.-H. Chen; J. F. Driscoll, Combust. Flame 86 (4) (1991) 347-358.
[3] S. Yuasa, Combust. Flame 66 (2) (1986) 181-192.
[4] S. F. Ahmed; R. Balachandran; T. Marchione; E. Mastorakos, Combust. Flame 151 (1–2) (2007) 366-385.
[5] F. Kiesewetter; M. Konle; T. Sattelmayer, J. Eng. Gas Turb. Power 129 (4) (2007) 929-936.
[6] D. Galley; S. Ducruix; F. Lacas; D. Veynante, Combust. Flame 158 (1) (2011) 155-171.
[7] M. Stöhr; C. M. Arndt; W. Meier, Proc. Combust. Inst. 35 (3) (2015) 3327-3335.
[8] V. D. Milosavljevic; A. M. K. P. Taylor; J. H. Whitelaw, Combust. Flame 80 (2) (1990) 196-208.
[9] C. O. Iyogun; M. Birouk; J. A. Kozinski, Fuel 90 (4) (2011) 1416-1423.
[10] A. Olivani. Thermo-fluid-dynamic Analysis of Methane/Hydrogen/Air Mixtures Under Reacting Conditions by Laser Diagnostics. PhD Thesis, Politecnico di Milano - Université d'Orléans, 2006.
[11] F. Cozzi; A. Coghe, Exp. Thermal Fluid Sci. 43 (0) (2012) 32-39.
[12] P. Palies. Dynamique et instabilités de combustion des flammes swirlées. PhD Thesis, Ecole Centrale des Arts et Manufactures, 2010.
[13] S. Candel; D. Durox; T. Schuller; P. Palies; J.-F. Bourgouin; J. P. Moeck, Comptes Rendus Mécanique 340 (11–12) (2012) 758-768.
[14] T. Lieuwen, Unsteady Combustor Physics, Cambridge, 2012.
[15] T. Boushaki; J. C. Sautet; L. Salentey; B. Labegorre, Int. Com. Heat Mass Transfer 34 (1) (2007) 8-18.
[16] N. Merlo; T. Boushaki; C. Chauveau; S. de Persis; L. Pillier; B. Sarh; I. Gökalp, Energy Fuels 27 (10) (2013) 6191-6197.
[17] H. S. Zhen; C. W. Leung; C. S. Cheung, Applied Energy 88 (9) (2011) 2925-2933.
[18] P. Bělohradský; P. Skryja; I. Hudák, Energy 75 (2014) 116-126.
[19] J. M. Beér; N. A. Chigier, Combustion Aerodynamics, Applied Science Publishers, London, England, 1972.
[20] N. Syred; J. M. Beér, Combust. Flame 23 (2) (1974) 143-201.
[21] S. C. Crow; Champagn.Fh, J. Fluid Mech. 48 (3) (1971) 547-591.
[22] D. Han; M. G. Mungal, Combust. Flame 124 (3) (2001) 370-386.